Available online at www.sciencedirect.com
SCIENCE DIRECT®
Pergamon
Acta Materialia 51 (2003) 3985–3997
Acta MATERIALIA
www.actamat-journals.com

Nano-indentation fracture test of $Pb(Zr_{0.52}Ti_{0.48})O_3$ ferroelectric thin films

X.J. Zheng [a,*], Y.C. Zhou [a], J.Y. Li [b]

[a] *Institute of Fundamental Mechanics and Material Engineering, Xiangtan University, Xiangtan, 411105, China*
[b] *Department of Engineering Mechanics, University of Nebraska-Lincoln, Lincoln, NE 68588-0516, USA*

Received 2 November 2002; received in revised form 3 April 2003; accepted 9 April 2003

Abstract

In this paper, we propose an elastic groundsill beam model with piezoelectric effect considered to assess the interfacial adhesion of ferroelectrics thin films, complemented and validated by nano-indentation fracture test on $Pb(Zr_{0.52}Ti_{0.48})O_3$ (PZT) thin films. It was observed that the hardness and elastic modulus of thin films depend on the indentation depth. It was also observed from the load-indentation depth curves and atomic force microscopy (AFM) images that the fracture failure of PZT thin films induced by nano-indentations can be divided into three typical stages: no damage, bulging and spallation. The delamination of thin film systems was modeled as an interfacial crack propagation problem, with the energy release rate determined from the elastic groundsill beam model. Good agreement was observed between the indentation load and the radius of the largest imprint. For PZT thin films deposited on single Si substrate with thickness of 350 nm and 450 nm, the energy release rates per unit new crack area are in the range of 3.4~52.4 J/m^2 and the phase angles are constant of 13.4°. The corresponding mode I and mode II stress intensity factors are in the range of $K_I = 0.4–1.6 MPa{\cdot}m^{1/2}$ and $K_{II} = 0.6–2.2 MPa{\cdot}m^{1/2}$.

Keywords: Nano-indentation; PZT thin film; Composite beam theory; Interfacial adhesion

1. Introduction

Since the emergence of thin and thick films at the end of 1970s and their subsequent applications in microelectromechanical systems (MEMS), there has been continuous effort for materials development and technology innovation in this field, leading to a significant number of industrial and commercial applications [1]. The basic premise behind MEMS concept is that the high volume production and low unit cost achieved by the microelectronics industry over the past 50 years can also be accomplished in devices where mechanical and electrical components are integrated into a single silicon chip or equivalent structure [2]. One of the major concerns of MEMS, however, is its relatively poor reliability caused by the delamination, brittle fracture and fatigue degradation of multilayer thin film structures [3,4], where interfacial adhesion plays a critical role. Interfacial adhesion is also an important measure of thin film brittle-

* Corresponding author. Tel.: +86 073 282 93030; fax: +86 073 282 92468
E-mail address: xj_zheng2002@hotmail.com (X.J. Zheng).

1359-6454/03/$30.00
doi:10.1016/S1359-6454(03)00208-8

ness, and generally speaking, harder films are more brittle and are more easily damaged [5].

The indentation test has long been applied to quantitatively assess the adhesion of film-substrate systems. Conventional micro-indentation technique [6–8] based on radial cracking induced by a sharp indenter, however, cannot be used to measure the interfacial adhesion of thin films, because the indentation depth at the radial cracking threshold load, below which cracking does not occur, exceeds 10% of the film thickness so that the elastic-plastic zone may expand to the substrate. The plastic zone material is incompressible and still transmits stresses to the elastic material outside the elastic-plastic boundary. Using radial cracking however would be inappropriate for measuring a delamination process. Furthermore, under shallow indentation depths, it is difficult to measure a radial crack length even with scanning electron microscope (SEM). These difficulties can be partially overcome by a nano-indentation technique developed by Kriese et al. [9] and Thouless [10], from which the adhesion of thin films can be measured semi-quantitatively. The scratch test is also widely used to quantitatively evaluate the adhesion of thin films to substrates [11,12], despite the lack of a fully satisfactory analytical model. The concepts of linear elastic fracture mechanics were used in the theoretical models of Thouless et al. [13] and DeBoer et al. [14,15], and were subsequently applied to analyze many nano-indentation problems. For example from the load-displacement curves and the fractographic photos obtained in nano-indentation test, Li and Bhushan [16,17] derived some important parameters to evaluate the interface fracture toughness of ultra-thin amorphous carbon coatings, including interfacial crack length and largest imprint of residual mark. Interfacial critical energy release rate for ceramic-ceramic systems has also been calculated from cross-sectional nano-indentation test (CSN) based on the elastic plate theory [18].

$Pb(Zr_xTi_{1-x})O_3$ (PZT) thin film is an important ferroelectric system with potential applications in MEMS, but the above-mentioned models can not be used to analyze the interfacial adhesion and indentation fracture of ferroelectrics thin films accurately because of the piezoelectric effect. The description of fracture toughness of a poled piezoelectric ceramic is very complicated, involving fracture toughness measured perpendicular and parallel to the poling direction [19–22]. Giannakopoulos and Suresh [23] have recently developed an indentation theory for bulk piezoelectric materials, and the analytical solutions are in good agreement with finite-element simulations. Yet to the best knowledge of authors, there is no measurement of interfacial adhesion for PZT thin film reported in literature. Due to the size-effects and the constraint of substrate, the properties of thin film are expected to be different from those of bulk materials.

In this paper, we propose an elastic groundsill beam model to evaluate the interfacial adhesion of PZT thin films, characterized by energy release rate per unit crack area in nano-indentation test when the largest indentation depth is close to the film thickness. The piezoelectric effects are fully considered in the model. To validate the model we conducted nano-indentation fracture test on PZT films deposited on single Si substrate by metal organic decomposition (MOD), using a cube corner indenter and atomic force microscopy (AFM). During the experiment no radial cracks were found on the indentation surface and the thin film around indenter had bulged upwards. The spallations of the thin film were observed when indentation depths exceeded 13% of the film thickness and when the diamond indenter penetrated through the thin film into the substrate. Interfacial delamination is approximately consisted of the classical mode I and mode II cracks and the corresponding mode II crack dominates the interfacial crack in the ferroelectrics thin films. The relationship between indentation load and residual indentation mark obtained from the experiment are in good agreement with our theoretical calculations.

2. Theoretical model

2.1. Indentation analysis of thin film

We first present a general theory for the axisymmetric indentation of transversely isotropic piezoelectric solids, governed by the following constitutive, equilibrium, and field equations

$$\begin{cases}\sigma_{ij} = c_{ijkl}\varepsilon_{kl} - e_{kij} \\ E_k D_i = e_{ikl}\varepsilon_{kl} + \in_{ik} E_k \end{cases}$$
$$\begin{cases}\sigma_{ij,j} = 0 \\ D_{i,i} = 0 \end{cases} \quad (1)$$
$$\begin{cases}\varepsilon_{ij} = (u_{i,j} + u_{j,i})/2 \\ E_i = -\phi_{,i} \quad . \end{cases}$$

In Eq. (1), σ_{ij},D_i,ε_{ij},u_i,E_i and ϕ are stress, electric displacement, strain, displacement, electric field and electric potential, respectively, and c_{ijkl},ε_{ik},e_{kij} are elastic, dielectric and piezoelectric constants, respectively. We consider the normal indentation of a piezoelectric thin films as shown in Fig. 1(a), where h, H, 2α and P_0 are thin film thickness, substrate thickness, apex angle and indentation load, respectively, and $2c$ is the largest imprint made on the surface of the film by the indenter. Using Eq. (1), combined with the assumption that the indenter is an insulator and does not reach the substrate, we have the relationship between the indentation load P_0 and the largest imprint $2c$ derived by Giannakopoulos and Suresh [19],

$$P_0 = \pi c^2 \cot\alpha \frac{M_8M_5 - M_7M_6}{M_1M_8 - M_2M_7}, \quad (2)$$

with the displacement $u_z(c,0)$ in z direction and electric potential $\phi(r,0)$ given by,

$$u_z(c,0) = (\frac{\pi}{2} - 1)c\cot\alpha, \quad (3)$$

$$\phi(r,0) = \cot\alpha \frac{h(M_3M_8 - M_4M_7)}{\pi(M_1M_8 - M_2M_7)}(\frac{\pi}{2}\cot\alpha - \frac{r}{c}), \quad (4)$$

where polar coordinate system is adopted. In Eq. (2), $M_I(I = 1,2\ldots8)$ are the parameters determined from materials properties [19]. Because both the film thickness h and indenter contact region size c are in the nanometer scale, we make the following approximations

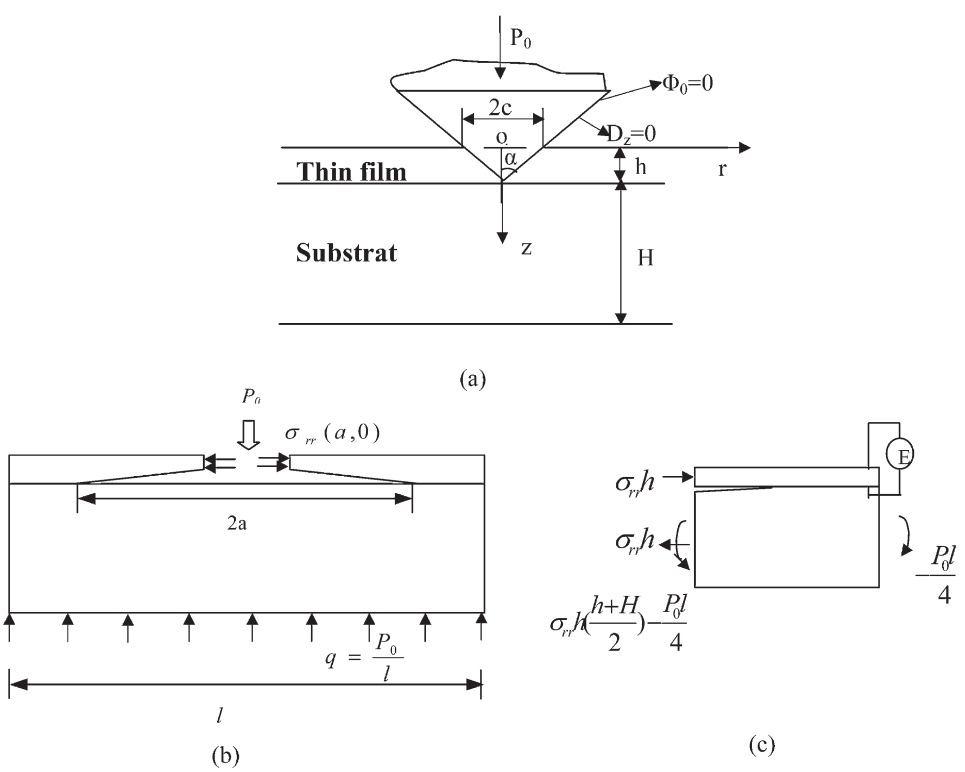

Fig. 1. (a) The schematic of the normal indentation of piezoelectric thin film materials; (b) Simplification of the elastic groundsill beam model; (c) Equivalent edge loading.

$$\frac{\partial u_r}{\partial z} = \frac{\Delta u_r}{h} = \frac{u_r(r,0)}{h}, \frac{\partial u_z}{\partial r} = \frac{\Delta u_z}{c} = \frac{u_z(c,0)}{c}, \tag{5}$$

$$E_z = -\frac{\partial \phi}{\partial z} = -\frac{\phi(r,0)}{h}. \tag{6}$$

We also have the following mechanical boundary conditions,

$$\begin{cases} u_z(r,0) = h-(c-r)\cot\alpha, \\ \sigma_{rz}(r,0) = 0, \sigma_{zz}(r,0) = 0; r > c \end{cases}. \tag{7}$$

and electric boundary conditions

$$D_z(r,0) = 0; r \geq 0. \quad D_z(r,h) = 0; r \geq 0. \tag{8}$$

Combining the shear strain on the surface of the film $\gamma_{rz} = e_{15}E_r/c_{44}$ with Eqs. (3)–(5) and Eq. (1), the displacement in r direction on the surface of the film could be obtained,

$$u_r(r,0) = \frac{e_{15}}{c_{44}}\frac{\phi_q h}{c} - \left(\frac{\pi}{2}-1\right)h\cot\alpha, \tag{9}$$

where

$$\phi_q = \frac{M_8M_5 - M_7M_6}{M_1M_8 - M_2M_7}\cot\alpha. \tag{10}$$

Combining the constitutive Eq. (1) and boundary conditions (7) and (8), the surface strain ε_{rr} can be obtained. Substituting Eqs. (3)–(6) and (9) into the constitutive relations and geometric equations, the fields in the indentation region can be obtained as,

$$E_z = -\frac{\phi_q}{h}\left(\frac{\pi}{2}\cot\alpha - 1\right), \tag{11}$$

$$\varepsilon_{zz} = -\frac{(e_{33}e_{31} + \in_{33}c_{13})\phi_q}{(c_{33}e_{31} - c_{13}e_{33})\ h}\left(\frac{\pi}{2}\cot\alpha - 1\right), \tag{12}$$

$$\varepsilon_{\theta\theta} = \frac{e_{15}}{c_{44}}\frac{\phi_q h}{c^2} - \left(\frac{\pi}{2}-1\right)\frac{h\cot\alpha}{c}, \tag{13}$$

$$\varepsilon_{rr} = \left[\frac{(e_{33}^2 + \in_{33}c_{33})1}{(c_{33}e_{31} - c_{13}e_{33})h}\left(1-\frac{\pi}{2}\cot\alpha\right)\right. \tag{14}$$

$$\left. -\frac{e_{15}h}{c_{44}c^2}\right]\phi_q + \frac{h}{c}\left(\frac{\pi}{2}-1\right)\cot\alpha.$$

Substituting Eq. (11)–(14) into the constitutive relation (1), the stress σ_{rr} in the indentation region of the thin film can be obtained as,

$$\sigma_{\mathrm{rr}} = c_{11}\varepsilon_{rr} + c_{12}\varepsilon_{\theta\theta} + c_{13}\varepsilon_{zz} - e_{31}E_z. \tag{15}$$

2.2. Constitutive equations of thin film/substrate system

We then present an elastic groundsill beam model as shown in Fig. 1(b) to describe the indentation fracture characteristics of thin films, where the indentation depth is assumed to be close to the film thickness. When $\eta = \frac{h}{H} \longrightarrow 0$, we can approximately apply Eq. (8) to the whole region of the thin film to obtain the following relationship between strain and electric field in the thin film

$$E_z = -\frac{e_{31}}{\in_{33}}\varepsilon_{rr}. \tag{16}$$

We further assumed that σ_{rr} and u_r are uniform across the thickness of the thin film since the film thickness is very small compared with its length, so that

$$\sigma_{\mathrm{rr}} = \left(c_{11} - \frac{c_{13}^2}{c_{33}}\right)\varepsilon_{rr} - \left(e_{31} - \frac{c_{13}e_{33}}{c_{33}}\right)E_z. \tag{17}$$

Substituting Eq. (16) into the constitutive relationship (17), we have

$$\sigma_{\mathrm{rr}} = \left(c_{11} - \frac{c_{13}^2}{c_{33}} + \frac{e_{13}^2}{\in_{33}} - \frac{c_{13}e_{13}e_{33}}{c_{33}\in_{33}}\right)\varepsilon_{rr}, 0 \leq z \leq h. \tag{18}$$

We also assumed that the substrate is isotropic governed by the constitutive equation,

$$\sigma_{\mathrm{rr}} = \frac{8\mu_2}{\kappa_2 + 1}\varepsilon_{rr},\ h \leq z \leq h + H, \tag{19}$$

which is derived from the composite beam theory, with $\kappa_2 = 3-4\nu_2, \nu_2$ and μ_2 being the Poisson's ratio and shear modulus of substrate, respectively. The strain could be written as, $\varepsilon_{rr} = \varepsilon_{rr}^0 + z^*k$, where ε_{rr}^0 and k are the strain and curvature at substrate's mid-plane, and z^* is the distance from this mid-plane to the point we are considering.

2.3. Stress intensity factors and the energy release rates

We next consider the interface crack problem as shown in Fig. 1(c) using the theory of composite

beam. The interface crack tip singularity would be controlled by equivalent edge stress P and bending moment M [24], given by

$$P = \sigma_{rr}h + \Omega_1\frac{P_0 l}{4}, \tag{20}$$

$$M = \Omega_2\frac{P_0 l}{4}. \tag{21}$$

where $2a$ and l are interfacial crack length and equivalent beam length of the indentation sample, respectively. The parameters Ω_1 and Ω_2 are related with the thickness and material properties of the thin film and substrate, listed in Appendix A. The energy release rate of interface crack in a piezoelectric material is controlled by the stress intensity factors K_1, K_2, K_3 and electric intensity factor K_4 [25]. Due to the electrical boundary condition (8), the electric intensity factor K_4 is zero, so is the stress intensity factor K_3. Thus the problem of interface crack in piezoelectric thin film reduces to a pure elastic interface crack problem, and the interface intensity factors K_1 and K_2 reduce to the classical mode I and mode II factors K_{I} and K_{II},

$$K_{\mathrm{I}} = \frac{1}{\sqrt{2}}\left[Ph^{-1/2}\cos\omega + 2\sqrt{3}Mh^{-3/2}\sin\omega\right], \tag{22}$$

$$K_{\mathrm{II}} = \frac{1}{\sqrt{2}}\left[Ph^{-1/2}\sin\omega + 2\sqrt{3}Mh^{-3/2}\cos\omega\right], \tag{23}$$

where the angle ω is a function related with the Dundurs' parameters α and β [24], $\omega = 53.3°$ with α and β given by $\alpha = \dfrac{\Gamma(\kappa_2+1)-(\kappa_1+1)}{\Gamma(\kappa_2+1)+(\kappa_1+1)}$, $\beta = \dfrac{\Gamma(\kappa_2-1)-(\kappa_1-1)}{\Gamma(\kappa_2+1)+(\kappa_1+1)}$, $\Gamma = \dfrac{\mu_1}{\mu_2}$, $\kappa_i = 3-4\nu_i$, (i = 1,2), where ν_i,μ_i are Poisson's ratio and shear modulus of thin film and substrate, respectively, with the subscripts 1 and 2 referring to film and substrate. The energy release rate per unit new crack area can be then written in terms of the complex stress intensity factor,

$$G = \frac{c_1 + c_2}{16\cosh^2\pi\varepsilon}|\mathbf{K}|^2, \mathbf{K} = K_{\mathrm{I}} + iK_{\mathrm{II}} \tag{24}$$

with the phase angle ψ given as

$$\psi = \tan^{-1}(K_{\mathrm{II}}/K_{\mathrm{I}}), \tag{25}$$

where the bimaterial constant is given as $\varepsilon = \dfrac{1}{2\pi}\ln\dfrac{1-\beta}{1+\beta}$, and the parameters c_1, c_2 are defined in Appendix A.

3. Experimental procedure

3.1. Sample preparation

To validate our theoretical model we carried out the following experiment. PZT thin films were prepared by MOD method, where the precursor compounds used were $Zr(OCH_2CH_2CH_3)_4$, $Ti(OCH_2CH_2CH_3)_4$ and $Pb(CH_3COO)_2{\cdot}3H_2O$, all in CH_3COOH,$CH_3CH_2CH_2OH$ solution, and the rotational speed of spin coating was 3000 rpm. In this process, the wet films were roasted for 3–5 mins on hot desk at 260 °C, so that the dissolvent with a low boiling point could be volatilized and dry films could be obtained. The dry films were then put into a quartz boat at 750 °C for 10 min and the thermal decomposition was annealing at 650 °C for 3 min by the rapid treatment annealing (RTA). By controlling the time of spin coating PZT films with different thickness of 500 nm, 450 nm and 300 nm were prepared. Because it is very difficult to obtain good ferroelectric thin films directly on a silicon substrate due to interface adhesion [1,26,27], we chose $Pt/TiO_2/SiO_2/Si(100)$ as the bottom electrodes in our preparation, as shown in Fig. 2. The samples were labeled as A, B,

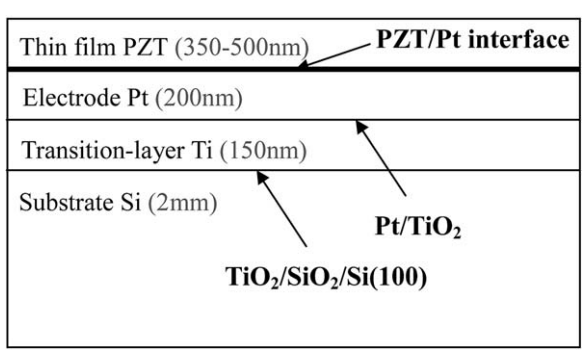

Fig. 2. The schematic mutil-layers structure of PZT ferroelectrics thin film.

C and D and their thickness and other experimental parameters are listed in Table 1.

3.2. Indentation procedure

Nano-indentations were carried out using a commercially available instrument CSEM, which monitored and recorded the dynamic load and displacement of the indenter. The three-sided indenter was driven perpendicularly into, then out of, the film. In order to understand indentation fracture process of PZT, we used three types of peak indentation loads to induce the fracture of the samples: less than 5 mN, 10–70 mN, and larger than 100 mN, and recorded the corresponding load-indentation depth curves. Each indentation experiment consisted of three steps: loading, holding the indenter at peak load for 10 s, and unloading completely. After the unloading, associated crack patterns were examined by AFM.

3.3. The determination of parameters

To determine necessary parameters for the theoretical model, we obtain elastic, piezoelectric and dielectric constants of PZT thin films from [19], listed here in Table 2. The interfacial crack length $2a$, the largest imprint $2c$ at the peak indentation load P_0, and the residual depth could be obtained from the AFM image. Therefore we can determine parameters$M_i(i = 1,2\ldots8)$, c_1, c_2, as well as Ω_1 and Ω_2. As a result the interfacial adhesion of PZT thin films could be determined from our theoretical model.

4. Experimental results and discussions

4.1. Load-displacement curves and indentation fracture patterns

In the indentation test, three ranges of indentation loads are applied to the samples: (1) low peak load smaller than 5 mN; (2) intermediate indentation load between 10 and 70 mN; (3) high peak load was high, larger than 100 mN. The typical load-displacement curves of indentations made on the sample C at three ranges indentation load are shown in Fig. 3(a)–(c), respectively. The typi-

Table 1
Experimental results for the delamination of PZT thin films induced by nano-indentation load

Sample	Thickness (nm)	Peak load (mN)	Fracture phenomenon	Radius of residual indent mark (nm)	Radius of delamination area (nm)	Energy release rate G(Ψ)(J/m²)
A	450	1		336.32		
		3		605.15	1082.55	
		10		993.21	3000.00	
		50	spallation	2784.39	4266.66	52.4
		100	spallation	3993.93	5333.33	
		150	spallation	4617.07	6666.66	
B	500	100	bugling	3335.10	5000.00	
		260	spallation	4701.09	7000.00	
		300	spallation	5604.79	7966.66	
C	350	2		417.82		
		30	bugling	2127.70	2900.00	42.7
		70	bugling	4697.70	4506.34	3.4
		150	spallation	5069.48	5952.38	
		260	spallation	5184.70	8000.00	
D	350	10	bugling	2127.70	2109.72	42.7
		30	bugling	2483.14	2750.00	28.3
		70	spallation	4572.11	4569.88	3.8
		150	spallation	6058.02	7446.08	
		260	spallation	6500.32	7978.72	

Table 2
The materials parameters of PZT thin film

Elastic coefficients (10^{10}Nm^{-2})					Piexoelectric coefficients (Cm^{-2})			Dielectric coefficients (10^{-10}Fm^{-1})		Poison's ratio		Elastic modulus of Si (10^{10}Nm^{-2})
c_{11}	c_{33}	c_{44}	c_{13}	c_{12}	e_{15}	e_{13}	e_{33}	ϵ_{11}	ϵ_{33}	ν_1	ν_2	E_2
13.9	11.5	2.56	7.43	7.78	12.7	−5.2	15.1	64.6	15.1	0.3	0.28	13

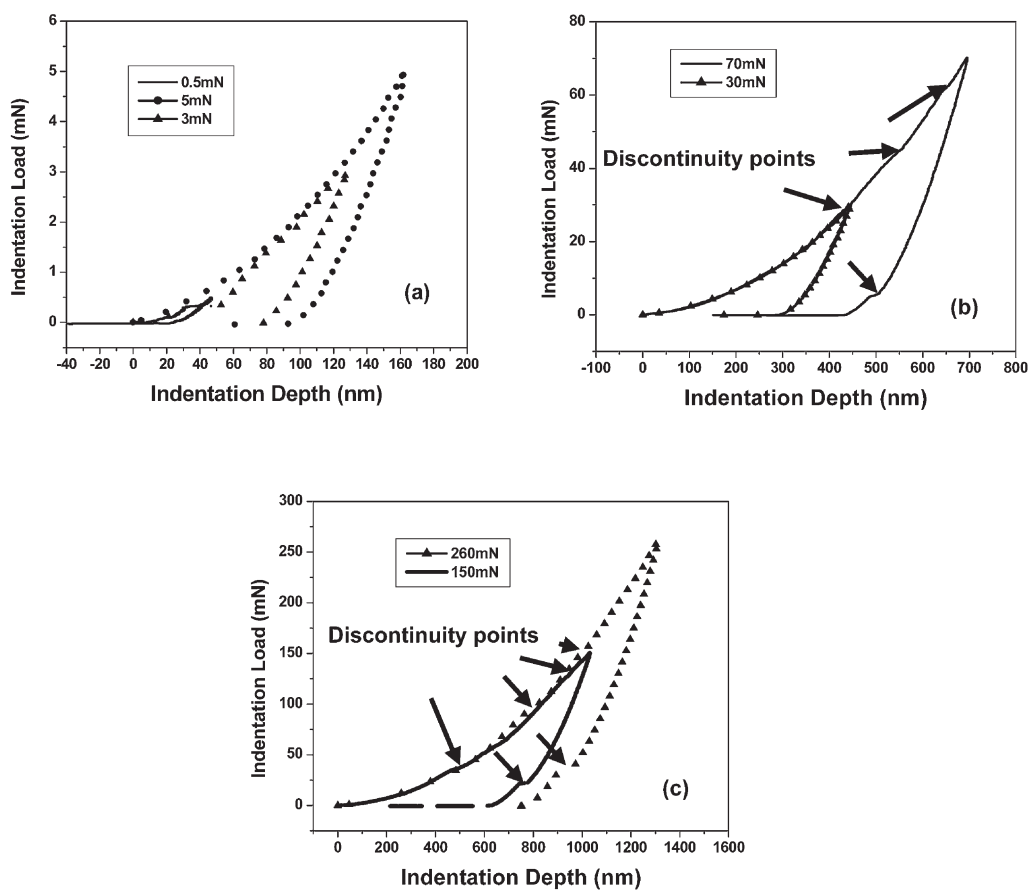

Fig. 3. The load-displacement curves of indentations made on the PZT thin films C at indentation loads of three ranges: (a) 0.5, 3 and 5 mN, (b) 30 and 70 mN, (c) 150 and 260 mN.

cal AFM images of indentation made at 2 mN on the sample C are shown in Fig. 4. The two-dimensional AFM image of the sample D at the peak load of 10 mN and the sample B at the peak load of 300 mN are shown in Fig. 5(a) and (b), respectively. From the AFM images and the load-indentation depth curves we can make the following observations on the failure process of PZT thin films: (1) When the peak load was very low, i.e., lower than 5 mN, the curves of load-indentation

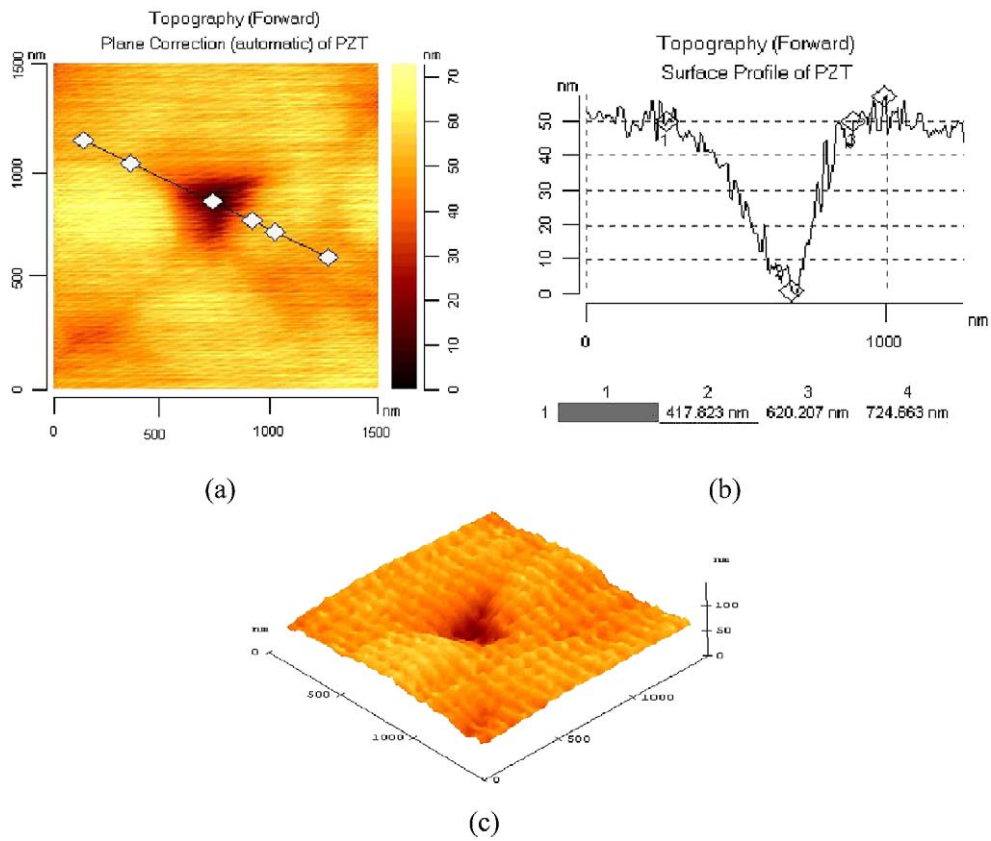

Fig. 4. Typical AFM images of indentation at 2mN: two-dimension images (a), the topography surface profiles (b), and three-dimension images (c) on the sample C.

depth shown in Fig. 3(a) were continuous and smooth. This suggests that the indenter did not penetrate through the thin film into the substrate during the indentation process, and no micro-cracks and bulging were observed, as shown in Fig. 4(a); (2) When the indentation load was intermediate, i.e., between 10 and 70 mN, the curves of load-indentation depth shown in Fig. 3(b) were discontinuous at one or two points on the loading curves, and were discontinuous at only one point on the unloading curves, as shown in Fig. 3(b). The first and second discontinuities on the loading curves corresponded to PZT/Pt interface and Pt/TiO_2 interface (see Fig. 2) that were penetrated by nano-indenter. In this case, only bulging was observed as shown in Fig. 5(a), which suggests that there were delamination and buckling but the interfacial cracks didn't propagate extensively. During the unloading only one discontinuity or a short step was observed (see Fig. 3(b) and (c)), possibly due to the residual deform of thin film. (3) When the peak load was high, i.e., higher than 100 mN, there were two and three discontinuous points on the loading curves, as shown in Fig. 3(c). As discussed before, the first and second discontinuities corresponded to PZT/Pt and Pt/TiO_2 interfaces that were penetrated by nano-indenter. The third discontinuity on the loading curves corresponded to Ti/Si interface (see Fig. 2) that was penetrated by nano-indenter. In this case, the spallation of the film was observed as shown in Fig. 5(b), indicating extensive propagation of interfacial cracks. Summarizing the experimental observation, we conclude that each discontinuity indicates the point where the nano-indenter was driven from one medium into another, and the propagation of interfacial cracks

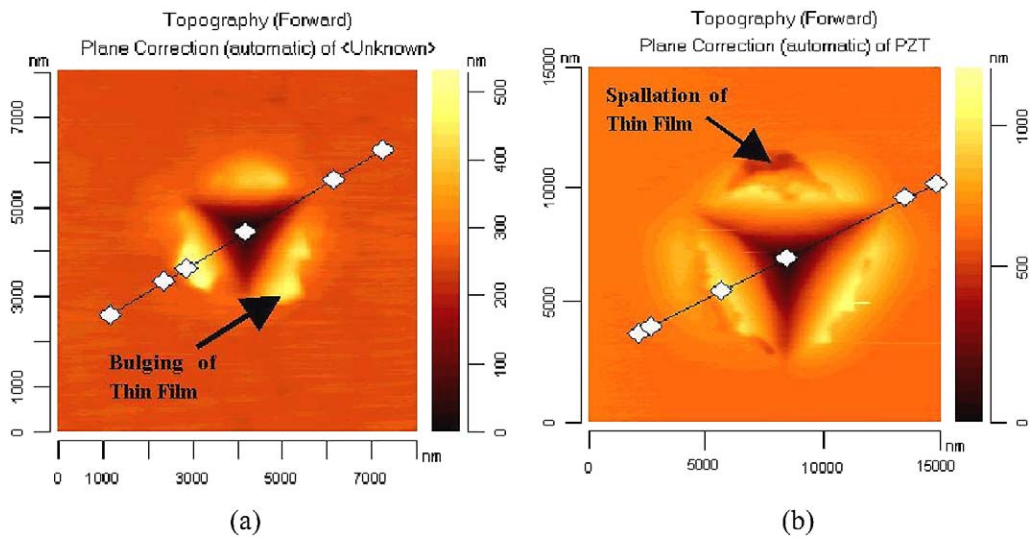

Fig. 5. (a) Bulging of the sample D at the indentation load 10 mN; (b) Spalling extension of the sample B at the indentation load 300 mN.

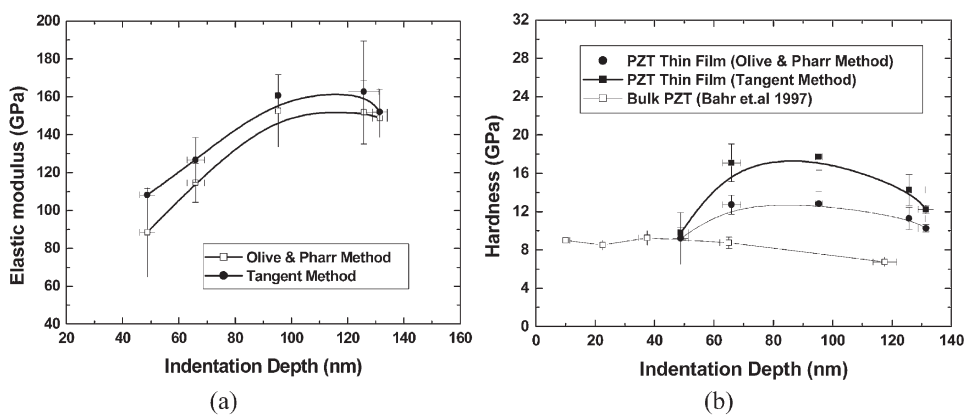

Fig. 6. The measurement of mechanical properties of the PZT thin films: (a) elastic modulus as a function of indentation depth; (b) hardness as a function of indentation depth; (c) the dependence of the hardness on indentation depth.

increases with increasing indentation load. The spallation and the corresponding discontinuity of load-indentation depth curve were also observed by other researchers [5,8].

The differences between the bulging shown in Fig. 5(a) and the spallation shown in Fig. 5(b) are distinguished in Table 1. By analyzing the AFM images including the topography surface profiles, two-dimensional and three-dimensional topographies, we can obtain the radius of the largest imprint c and the interfacial fracture area a. For example, in the topography surface profile Fig. 4(b) and (c), the distance between 1 and 3 were used to determine the radius of the largest imprint c, while the distance between 1 and 4 were used to determine the radius of the interfacial fracture area a. Since we assume the indentation depth is close to the thin film thickness in our model, we only used the experimental data obtained at the peak indentation loads less than 70 mN to assess the energy release rate per unit new crack area. All these results are listed in Table 1.

4.2. The elastic modulus and hardness of thin films

The elastic modulus and hardness of $Pb(Zr_{0.52}Ti_{0.48})O_3$ thin films could be determined from load-indentation depth curve by Oliver and Pharr method [28] or tangent method [29]. The elastic modulus and hardness of $Pb(Zr_{0.52}Ti_{0.48})O_3$ thin films versus the indentation depth are summarized in Fig. 6(a) and (b), respectively. It is observed that both hardness and elastic modulus are dependent on the indentation depth, and the values determined by Oliver and Pharr method [28] are significantly lower than those determined by tangent method. Comparing the results with the elastic modulus 68 GPa and the indentation hardness 9 GPa reported by Bahr et al. [3] for PZT bulk materials, it is observed that the elastic modulus and hardness of PZT thin films are significantly higher than those of PZT bulk materials. As clear from Fig. 6, the hardness of bulk PZT ceramic is approximately constant independent on the indentation depth. For $Pb(Zr_{0.52}Ti_{0.48})O_3$ ferroelectrics thin films, however, the relationship between the indentation hardness and indentation depth is parabolic. It is clear that the elastic modulus and hardness of PZT thin film increase with the indentation depth, and the maximum elastic modulus is 150 GPa. This cannot be a substrate effect, since the shallow indentation depths are less than 13% of the film thickness and both the layers of Pt and Ti (See Fig. 2) have elastic module less than 150 GPa. The increase may be caused by the thin transition layers Ti/Pt, or due to the increase in the stress necessary to operate dislocation sources [29].

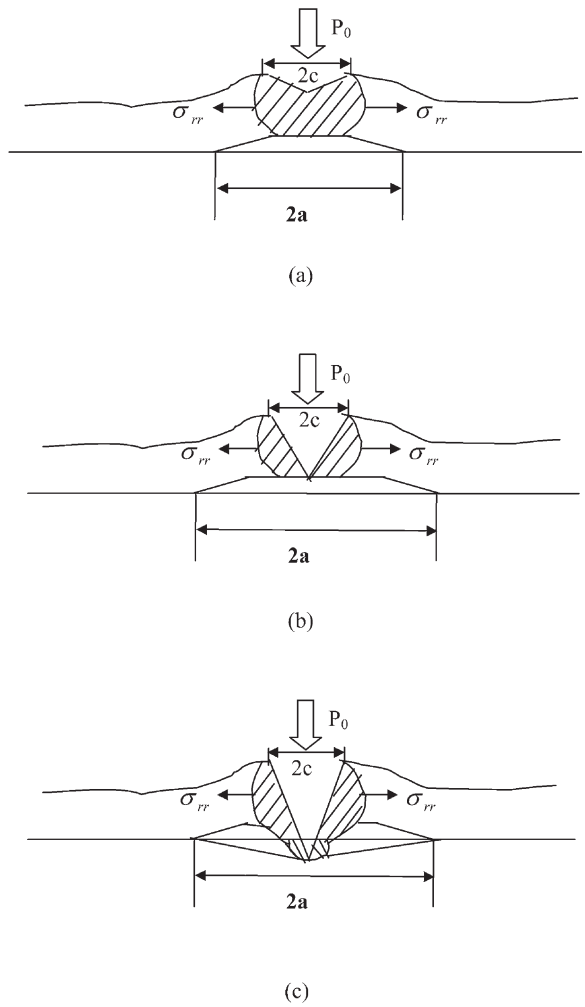

Fig. 7. Schematic of the interfacial fracture patterns corresponding to different indentation depths: (a) less than film thickness, (b) equal to film thickness, (c) larger than film thickness.

4.3. Fracture patterns and the validity of the theoretical model

The observed interfacial fracture patterns can be summarized in Fig. 7(a)–(c) corresponding to three range indentation loads. It is obvious that the elastic groundsill beam model in Fig. 1(b) only applies to the interfacial fracture pattern in Fig. 7(b) where the indentation depth is equal to thin film thickness. Generally speaking, interfacial delamination induced by bulging corresponds to the interfacial fracture pattern given in Fig. 7(a), while interfacial delamination induced by spalling corresponds to the case of Fig. 7(c). Indentation loads between 30 and 70 mN induce the indentation depths just about the PZT film thickness, therefore can be analyzed using our theoretical model. The experimental data for indentation load P_0 and the radius of the largest imprint c are compared with the theoretical results predicted by Eq. (2) in Fig. 8(a), where it is observed that the experimental points were near the theoretical curve but lower. When the indentation load was low, the theoretical relationship is in good agreement with experiment. However, when the

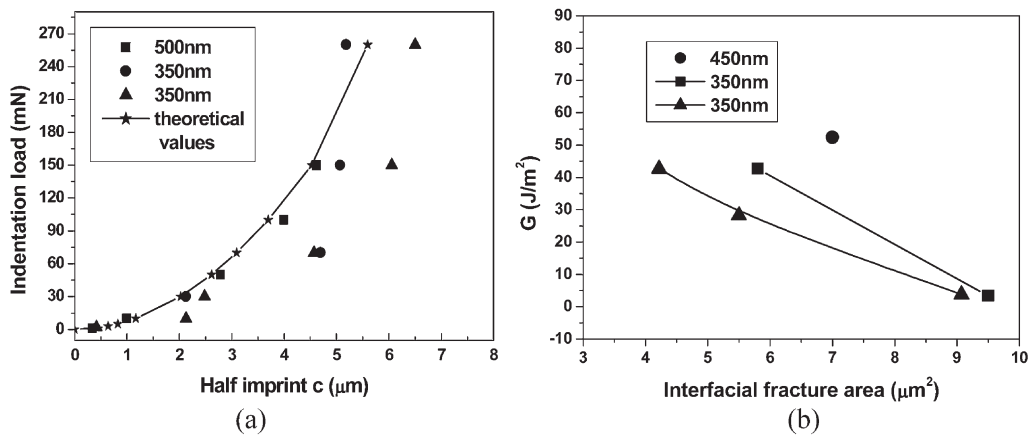

Fig. 8. (a) The relationship between indentation load and half imprint c. (b) The energy release rate per unit of new crack area for piezoelectric thin film $Pb(Zr_{0.52}Ti_{0.48})O_3$ as a function of interfacial fracture area.

indentation load was high, the difference between the experimental data and theoretical results was high. This is because the substrate starts to have effect on the indentation imprint when the indentation depth was larger than the thin film thickness.

4.4. Energy release rate per unit of new crack area

After determining the radius of the residual indent mark region c, the interface intensity factors K_1, K_2, energy release per unit new crack area G, and the phase angle ψ can be calculated by Eqs. (22)–(25), respectively. The interfacial fracture area is determined by interfacial crack length 2a and the largest imprint 2c with the assumption that the interfacial fracture region was circular. The energy release rate per unit new crack area determined in this manner is listed in Table 1. The energy release rate versus the interfacial fracture area is shown in Fig. 8(b), which showed that the energy release rate decreased as the interfacial crack length increased and similar phenomenon was also observed by Kriese et al. [9]. The energy release rate per unit new crack area for PZT ferroelectrics thin films with thickness of 350 and 500 nm are in the range of 3.4–52.4 J/m^2, and film with thickness of 350 nm has lower values. The phase angles are constant at 13.4°. The corresponding mode I and mode II stress intensity factors are in the range of K_{I} = 0.4–1.6MPa·$m^{1/2}$ and K_{II} = 0.6–2.2MPa·$m^{1/2}$. It is clear that the stress intensity factor for mode II crack is larger than that for mode I crack.

5. Concluding remarks

We proposed a model to measure interfacial adhesion in ferroelectric thin films. An elastic groundsill beam model taking into account the piezoelectric effect is developed to describe the interfacial crack for ferroelectrics thin films when the indentation depth is close to the film thickness. The energy release rate, the interface fracture stress intensity factors, and the phase angle were derived using the composite theory and elastic groundsill beam model, expressed in terms of the equivalent edge stress P and bending moment M. The model was validated by nano-indentation tests made on PZT thin films, where the elastic modulus and hardness of PZT thin films were determined from load-indentation depth curves, and energy release rate and stress intensity factors were calculated. The energy release rate per unit new crack area for PZT thin films with thickness of 350 and 500 nm are in the range of 3.4–52.4 J/m^2 and phase angles are constant of 13.4°. The corresponding mode I and mode II stress intensity factors are in the range of K_{I} = 0.4–1.6MPa·$m^{1/2}$ and K_{II} = 0.6–2.2MPa·$m^{1/2}$. Good agreement between experimental data and the theoretical results was observed.

Acknowledgements

We gratefully acknowledge the support of NNSF of China (No. 10072052).

Appendix A

The parameters Ω_1 and Ω_2 in Eqs. (20) and (21) are given as,

$$\Omega_1 = \frac{\sum}{I_0}\left(\frac{1}{\eta} - \Delta + \frac{1}{2}\right) \tag{A1}$$

$$\Omega_2 = \frac{\sum}{12 I_0} \tag{A2}$$

where,

$$\eta = \frac{h}{H}, \sum = \frac{c_2}{c_1},$$

$$c_1 = \frac{8 c_{33} \in_{33}}{(c_{11} c_{33} \in_{33} - c_{13}^2 \in_{33} + c_{33} e_{13}^2 - c_{13} e_{13} e_{33})},$$

$$c_2 = \frac{\kappa_2 + 1}{\mu_2} \tag{A3}$$

$$\Delta = \frac{1 + 2\Sigma\eta + \Sigma\eta^2}{2\eta(1 + \Sigma\eta)} \tag{A4}$$

$$I_0 = \frac{1}{3}\left\{\Sigma\left[3\left(\Delta - \frac{1}{\eta}\right)^2 - 3\left(\Delta - \frac{1}{\eta}\right) + 1\right] + 3\frac{\Delta}{\eta}\left(\Delta - \frac{1}{\eta}\right) + \frac{1}{\eta^3}\right\} \tag{A5}$$

Here, subscripts 1 and 2 refer to piezoelectric thin film and single Si substrate, respectively.

References

[1] Haertling GH. J Am Ceram Soc 1999;82:797.
[2] Spearing SM. Acta Metall 2000;48:179.
[3] Bahr DF, Robach JS, Wright JS, Francis LF, Gerberich WW. Mater Sci Eng 1999;A259:126.
[4] Diao DF, Kato K, Hokkirigawa K. AMSE Journal of Tribology 1994;116:860.
[5] Dunn ML, Taya M. Int J Solids Structures 1993;30:161.
[6] DeBoer MP, Gerberich WW. Acta Metall 1996;44:3177.
[7] Rosenfield LG, Ritter JE, Lardner TJ, Lin MR. J Appl Phys 1990;67:3291.
[8] Steinmann PA, Hintermann HE. J Vac Sci Technol 1989;A7:2267.
[9] Kriese MD, Boismier DA, Moody NR, Gerberich WW. Nanomechanical fracture-testing of thin films. Eng Fract Mech 1998;61:1–20.
[10] Thouless MD. An analysis of spalling in the microscratch test. Eng Fract Mech 1998;61:75–81.
[11] Blees MH, Winkelman GB, Balkenende AR, den Toonder JMJ. The effect of friction on scratch adhesion testing: application to s sol-gel coating on polypropylene. Thin Solid Films 2000;359:1–13.
[12] Venkataraman SK, Nelson JC, Hsieh AJ, Kohlstedt DL, Gerberich WN. Continuous microscratch measurements of thin film adhesion strengths. J Adhes Sci Technol 1993;7:1279–92.
[13] Thouless MD, Hutchinson JW, Liniger EG. Plain-strain, bulking-driven delamination of thin films: model experiments and mode-II fracture. Acta Metall 1992;40:2639–49.
[14] DeBoer MP, Gerberich WW. Microwedge indentation of the thin film fine line--I. Acta Metall 1996;44:3169–75.
[15] DeBoer MP, Kriese MD, Gerberich WW. Investigation of a new fracture mechanicals specimen for thin film adhesion measurement. J Mater Res 1997;12:2673–85.
[16] Li XD, Bhushan B. Evaluation of fracture toughness of ultra-thin amorphous carbon coatings deposited by different deposition techniques. Thin Solid Films 1999;355–356:330–6.
[17] Li XD, Bhushan B. Measurement of fracture toughness of ultra-thin amorphous carbon films. Thin Solid Films 1999;315:214–21.
[18] Sanchez JM, El-Mansy S, Sun B, Scherban T, Fang N, Pantuso D, Ford W, Elizalde MR, Martinez-Esnaola JM, Martin-Meizosa A, Gil-Sevillano J, Fuentes M, Maiz J. Cross-sectional nanoindentation: a new technique for thin film interfacial adhesion characterization. Acta Mater 1999;47(17):4405–13.
[19] Mehta K, Virkar A. Fracture mechanisms in ferroelectric-ferroelastic lead zirconate titanate (Zr:Ti=0.54:0.46) ceramics. J Am Ceram Soc 1990;73(3):567–74.
[20] Uchino K. Piezoelectric actuators and ultrasonic motors. Boston: Kluwer Academic Press, 1997.
[21] Randall CA, Kim N, Kucara JP, Cao WW, Shrout TR. Intrinsic and extrinsic size effects in fine-grained morphotropic-phase-boundary lead zirconate titanate ceramics. J Am Ceram Soc 1998;81(3):677–88.
[22] Yang W. Mechatronic reliability. Beijing: Tsinghua University Press, Springer-Verlag, 2001.
[23] Giannaropoulos AE, Suresh S. Theory of indentation of piezoelectric materials. Acta Mater 1999;47:2153–64.
[24] Suo Z, Hutchinson JW. Interface crack between two elastic layers. I J Fract 1990;43:1–18.
[25] Suo Z, Kuo C-M, Barnett DM, Willis JR. Fracture mech-

anics for piezoelectric ceramics. J Mech Phys Solids 1992;40:739–65.
[26] Niwa K, Kotaka Y, Tomotani M, Ashida H, Goto Y, Otani S. Interface between electrode and PZT memory device. Acta Metall 2000;48:4755–62.
[27] Choi WK, Choi SK, Lee HM. Relationship between domain structure and film thickness in epitaxial $PbTiO_3$ films deposited on MgO(001) by reactive sputtering. J Mater Res 1999;14(12):4677–784.
[28] Oliver WC, Pharr GM. An improved technique for determining hardness and elastic modulus using load and displacement sensing indentation experiments. J Mater Res 1992;7:1564–83.
[29] Bhushan B. Handbook of micro/nanotribology. CRC Press Inc., 1995.